Characterization of Laser-Produced Plasma Density Profiles Using Grid Image Refractometry

Grid image refractometry (GIR)[1] is proposed as a new technique for determining the two-dimensional density profiles of long-scale-length laser-produced plasmas such as will be generated on the OMEGA Upgrade. Interferometry, which has been successfully used to diagnose smaller plasmas, is unsuited to these plasmas because of problems associated with high fringe counts and fringe blurring.

The distinctive feature of GIR is that an optical probe beam is broken up into "rays" by being passed through a grid before traversing the plasma. The refraction angles of these rays are measured by imaging the plasma at two or more object planes and are integrated to yield the phase front. For cylindrically symmetric plasmas the density profile is then determined using Abel inversion. The feasibility of GIR is illustrated here by an analysis of an experiment carried out at KMS Fusion. The inferred density profile is substantially larger than any previously reported using interferometry and compares quite closely with *SAGE* hydrodynamic simulations.

Introduction

A fundamental concern in the study of laser-plasma interactions is the characterization of the plasma density profile that results when one or more laser beams irradiate a solid target. Knowledge of quantities including the plasma density, scale length, and temperature is especially important for the understanding of stimulated plasma physics processes, which can lead to a reduction in the overall laser-target coupling efficiency and/or the production of energetic electrons that potentially preheat the fusion fuel. In addition, it is desirable to compare experimental density profiles with predictions of hydrodynamic simulations in order to check the accuracy of computer modeling, especially in two dimensions where there is a sparsity of experimentally determined density profiles. Such comparisons might also provide insight into different models of thermal transport in the underdense corona.

The primary diagnostic of plasma density profiles has for many years been interferometry. Typically a short, 0.26-μm optical probe beam, derived from frequency quadrupling a Nd:glass laser, has been used to diagnose electron densities (n_e) up to ~1×10^{21} cm^{-3}. Generally the plasma is cylindrically symmetric, and Abel inversion (see, for example, Refs. 2–4) has been used to obtain the two-dimensional density profile. (Regrettably, very few such two-dimensional profiles have ever been published.) Notable results from interferometry have included the observation of profile steepening for 1-μm laser wavelengths,[5,6] where the high spatial resolution of interferometry has allowed scale lengths of ~1 μm to be measured. However, plasmas of current interest are less amenable to interferometric characterization for a number of reasons—the primary reason being their size. Exploding-foil plasmas with density scale length L_n ~0.5–1 mm have been produced on lasers such as NOVA[7] at the Lawrence Livermore National Laboratory and OMEGA[8] at the University of Rochester, and plasmas with true reactor scale lengths ($L_n \gtrsim 1$ mm) have recently been produced on NOVA using foams and high-density gas targets.[9] Interferograms of these plasmas would contain hundreds of fringes with spacing d_F (in the plane of the plasma) ranging from a few microns to around a millimeter. (The minimum spacing $d_{\min}$ is approximately equal to $2F\lambda_p$, where F is the f number of the collection optics and λ_p is the probe wavelength, and the maximum spacing is comparable to the plasma scale length at the density corresponding to the outer fringe.) A large field of view would thus be required. Moreover, the fringe pattern can change very rapidly in time and be smeared out unless a sufficiently short probe beam is used.

To illustrate the limitations of plasma interferometry it is worth noting that, to the best of our knowledge, there are no reports in the literature of laser-produced plasma density profiles that have been determined from interferograms with over 20 fringes. (One fringe corresponds to a path length of 8 μm for a 0.25-μm probe and a plasma density of 10^{21} cm^{-3}.) In experiments in which small microballoon targets[5,6,10,11] or fiber tips[12,13] were irradiated with short laser pulses of 1-μm wavelength, ~5 fringes were typically observed. For 10-μm laser irradiation of somewhat bigger microballoons,[14] ~10 fringes were observed (after the subtraction of back-

ground fringes). In later experiments on the CHROMA laser, in which targets were irradiated at 0.5 μm and diagnosed with a four-frame holographic system,[15] 10–20 fringes were observed both for exploding-foil targets[16,17] and cryogenic microballoon targets.[18] Large fringe counts (up to ~75) were seen in other (unpublished) experiments on CHROMA and were often limited by blurring due to plasma motion and inhomogeneities. Of all the experiments cited here, only in the 10-μm case[14] were the two-dimensional density contours reported.

A further problem, not unique to interferometry but shared by all optical probing techniques, is that it is unrealistic to probe to (electron) densities higher than 1 (or possibly 2) $\times$ 10^{21} cm^{-3}. This density is independent of the plasma size but does depend (usually weakly) on the plasma shape. (Simple estimates of this density are given in Ref. 1.) While this allows probing to the critical density (n_c) for 1-μm radiation, information can generally be obtained only up to ~0.1–0.2 n_c for the short laser wavelengths ($\lambda \leq 0.35$ μm) of current interest. This is not a substantial concern since stimulated Raman scattering, one parametric process of great interest, occurs strongly at densities $n_e \sim 0.1$ n_c, and sometimes parametric processes at lower densities are also of interest.[19] Moreover, in the exploding-foil geometries that are often used for plasma physics experiments (see Ref. 8 and references therein), the density gradients tend to zero in the center of the plasma, the refractive limitation does not apply there, and higher densities can be diagnosed.

The long-scale-length plasmas generated on OMEGA[8] were diagnosed using a simple Schlieren technique in which the inner portion of the collection optic was blocked by a disk of f number F_s. Images of the plasma thus provided two contours of deflection angle, $\theta_{\min} = \tan^{-1}(2F_s)^{-1}$ and $\theta_{\max} = \tan^{-1}(2F)^{-1}$, where F is the f number of the collection optic. Comparison of these images with two-dimensional hydrodynamic/ray-tracing simulations using the code *SAGE*[20] showed good agreement, increasing confidence in the predicted density profiles. However, insufficient information was obtained to enable the density profile to be arrived at independent of simulations.

Grid image refractometry (GIR), as described in this article, is a more general Schlieren technique that can permit the independent experimental determination of density profiles. It permits, in principle, every contour of deflection angle (up to $\theta_{\max}$) to be obtained, thus providing sufficient information for the density profile to be inferred for plasmas with cylindrical symmetry. The term "refractometry" is used to describe the well-established technique whereby the refractive index $\mu(\mathbf{r})$ of an optical medium is inferred from the refraction angles $\Delta\theta(p)$ of a one- or two-dimensional set of probe rays parametrized by an impact parameter p. For the common case of cylindrical symmetry, Abel inversion of $\Delta\theta(p)$ to give $\mu(\mathbf{r})$ is straightforward.[3]

With GIR, the refraction angles are measured by passing an optical probe beam through a grid before it propagates through the plasma. An image of the grid is formed within the plasma with a relatively long depth of focus. The probe beam is effectively broken up into a two-dimensional set of "rays," one ray corresponding to each point on the grid. The collection optics are then used to form two or more images of the grid corresponding to different object planes within the plasma. The refraction angles of each ray (in the two orthogonal directions) may be determined simply from the difference between the apparent positions of the associated grid element in two object planes divided by the distance between those planes.

A wide variety of alternative methods for measuring the refraction angles have been reported. The technique closest to GIR is known as the "point-grid method" and is described by Vasil'ev.[21] Here a two-dimensional square grid is placed at an appropriate point in the path of the probe beam (after the medium being probed and near a focal plane of the imaging optics). Again, each grid point may be thought of as corresponding to a ray. By comparing the grid-point positions in the images taken with and without the optical medium present (the working and reference images, respectively), the ray deflection angles in each direction can be obtained from a knowledge of the parameters of the optical system. This was illustrated in Ref. 21 with a cylindrical medium (air flowing around a heated pipe) probed parallel to its axis. Essentially the same method was used by Gurfein *et al.* to measure the density profile of a very compressible fluid (near-critical CO_2) in the Earth's gravitational field,[22] and by Miyanaga *et al.*[23] and Benattar[24] to determine the density profile in the overdense region of a laser-produced plasma using x rays as the probing radiation. In Ref. 23, kilo-electron-volt x rays from a point source passed through a laser-irradiated spherical target, through a zone plate (used as a grid), and onto film; from the observed distortion of the image of the zone plate the ray refraction angles (up to 8 mrad) and hence the electron-density profile (10^{23}–10^{24} cm^{-3} with a scale length ~20 μm) were determined. A closely related technique, moiré deflectometry,[25] has also been demonstrated for x-ray

wavelengths.[26] Moiré deflectometry provides the ray refraction angles in one direction. A similar principle is embodied in Hartmann sensors used for the testing of optical surfaces.[27] Here the phase front is broken up into rays by being passed through a screen perforated with an array of holes; the ray deflection angles are then calculated from the ray locations in a far-field recording plane. Photothermal deflection provides yet another form of refractometry and has been used, for example, to diagnose the laser ablation of materials.[28] Here the whole-beam deflection is measured of a probe beam whose diameter is small in comparison with the scale length of the medium being probed. A separate shot is needed for each impact parameter, although a single shot suffices if the shape of the refractive index profile in the medium is known independently.

Interferometry may be considered to be a form of refractometry in which wave rather than geometrical optics are used to measure the refraction angle. The fringe spacing d_F determines the angle $\Delta\theta$ between the actual and reference wavefronts: for small angles, $d_F \approx \lambda_p / \Delta\theta$. In the approximation of weak refraction, integration of the refraction angle (or equivalently fringe counting) yields the phase front, although the case of strong refraction, where fringe distortion and ray crossing can occur, is more complicated.

One advantage of GIR is that the impact parameters of all probe rays are known. The point-grid and other methods described above are all diagnostics of the emerging wavefront, requiring the impact parameter of each ray to be inferred. Distortion of the fringe count and the apparent fringe positions due to small focusing errors (between the object plane of the probe beam and the symmetry axis of the irradiating laser) has been a major problem in plasma interferometry. GIR, however, is not sensitive to this error; indeed, in the data reduction reported here, no knowledge of the absolute location of any of the object planes was needed. For the diagnosis of long-scale-length plasmas, GIR can provide essentially the same density information as interferometry, but it does not suffer from the major drawbacks of interferometry. The micron spatial resolution of interferometry is lost, but this is not usually an important consideration for millimeter scale lengths.

In this article the GIR technique is illustrated by an experiment carried out at KMS Fusion on the CHROMA laser. Useful data were obtained from just one shot. From this data, it has been possible to extract very plausible density profiles that compare quite closely with two-dimensional hydrodynamic simulations using the code *SAGE*.

Experiment

The layout of the KMS experiment is shown schematically in Fig. 57.5(a). An incident laser of wavelength $\lambda_L = 527$ nm irradiated a 50-μm-thick solid CH disk target. The plasma was diagnosed using a short (~30-ps), 263-nm probe beam (of energy ~10 μJ) that was passed in the z direction through a copper-mesh grid, of spatial periodicity 50 μm × 50 μm, before passing through the plasma. The optical system relayed an image of the grid into the plasma, with unit magnification, onto the plane $z = z_0$ containing the incident laser axis, using a fairly slow, $f/10$, source lens. The refracted probe light was collected by an $f/2$ catadioptric reflector system[15] and relayed to a plane where it interfered with a reference beam and was recorded on holographic film. On reconstruction, an image of the grid was formed on the film plane with a magnification of ~10. The advantage of the holographic recording used was that by varying the position of the film plane, images were obtained corresponding to various different object planes (14 in total) within the plasma.

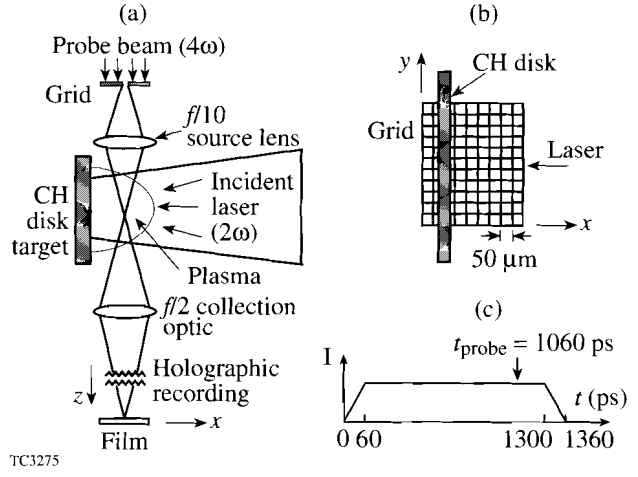

Figure 57.5
Schematic of GIR experiment carried out on the CHROMA laser at KMS Fusion. (a) Solid CH disk target, irradiated by a 527-nm laser. The plasma was diagnosed with a 263-nm probe beam with optics that relayed an image of a 50-μm grid into the plasma and then (holographically) onto film. (b) Grid as viewed by the probe beam. (c) Laser time history.

The grid location with respect to the disk target is shown in Fig. 57.5(b). [Unfortunately, due to a lack of comparison images from a plasma-free reference shot, the absolute location of the disk in the (x,y) plane and the y coordinate of the laser axis were not known.] The (x,y,z) coordinate system shown in Figs. 57.5(a) and 57.5(b) is used consistently throughout this article; thus the cylindrically symmetric *SAGE*

simulations are carried out with x the symmetry axis and y the radial direction.

The temporal history of the laser pulse, as modeled by *SAGE*, is shown in Fig. 57.5(c). It is essentially a flat pulse of 1.3-ns duration with the probe beam timed at 1.06 ns. The beam energy was 107 J and the beam diameter on target was d_0 ~ 400 μm. Since the exact on-target spatial profile was not known, simulations were carried out for two spatial shapes that should bracket the actual profile: (a) a flat profile truncated to zero at radius $d_0/2$, giving a laser intensity of 6.5×10^{13} W/cm^2 for $d_0 = 400$ μm, and (b) a Gaussian profile whose intensity falls to 10% of the peak at a radius $d_{90}/2$, truncated to zero at this radius, giving an on-axis intensity of 1.1×10^{14} W/cm^2 for $d_{90} = 400$ μm. (Simulations were also carried out with different spot diameters.)

Three representative images, resulting from holographic reconstruction and corresponding to different object planes, are shown in Fig. 57.6. The first image corresponds to an object plane closer to the grid ($z < z_0$) and the third to a plane closer to the collection optic ($z > z_0$). The left portion of the dark band is due to obscuration by the unirradiated target, which could present a width of >50 μm if not perfectly aligned. The right portion results from probe rays that are incident close to the target surface and are refracted through angles outside the *f*/2 cone of the catadioptric optic. The images have slightly different magnifications due to their different object planes.

A number of features may be seen in Fig. 57.6. The positions of the grid points behind the target appear to be unchanged from image to image. This is not surprising since simulations show that no significant plasma is expected to form behind the target. On the other hand, the grid points to the right of the target, especially those close to the target, shift to the right with increasing z. This shift is greater for grid points near the laser axis, resulting in a change of curvature between images that can be best perceived in the vertical line just to the right of the dark band. Image quality degrades toward the edge of the image, some (ideally square) grid images degrade into double images, and interference effects between neighboring grid elements are apparent. In image (c) there appears to be a caustic on the right edge of the dark band, pointing to an overlap of grid-point images resulting from strong refraction. In all the images there appears to be an up-down skew to the vertical lines: i.e., those on the right do not appear to be quite parallel to those behind the target. This is unlikely to result from an up-down asymmetry in the expanding plasma since the distortion persists (and may even be greatest) on the far right where the plasma density is the lowest. Rather, the distortion is presumed to be due to a nonuniformity in the grid or an aberration in the optical system. Qualitatively, then, most features of the images may be understood; however, digitization of the images is essential to enable GIR to provide quantitative information.

The principle of GIR is illustrated schematically in Fig. 57.7(a). Here, a set of parallel probe rays is shown incident on the plasma, one per grid element. A typical ray, which would appear to come from point P if the plasma were absent, is refracted through an angle θ_x in the (x,z) plane [and a corresponding angle θ_y in the (y,z) plane]. Depending on the

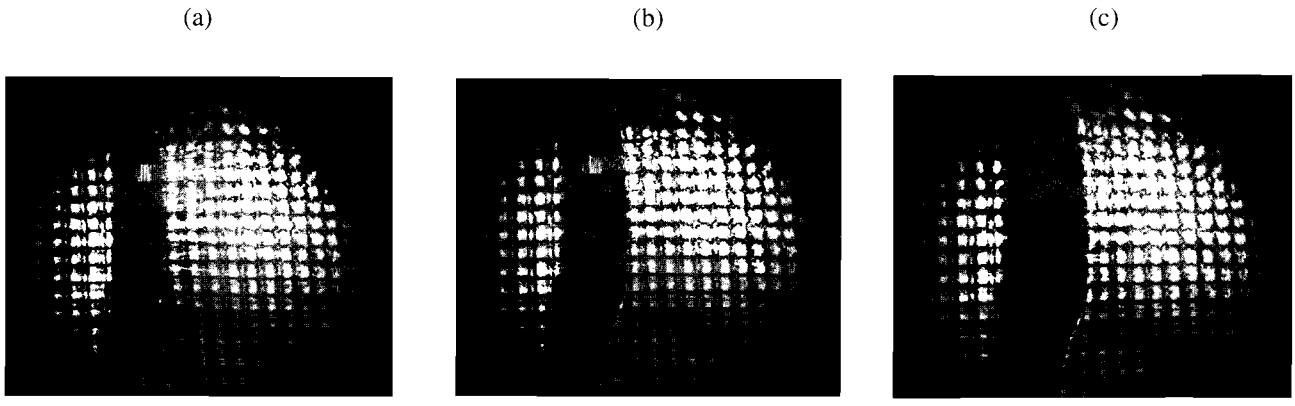

TC3089

Figure 57.6
Images after holographic reconstruction at object planes (a) $z = 200$ μm, (b) $z = 600$ μm, and (c) $z = 800$ μm, in the same orientation as Fig. 57.5(b). Image (b) corresponds approximately to the center of the plasma. The dark band is due partially to obscuration by the CH target and partially to refraction of probe rays close to the target surface through angles outside the *f*/2 cone of the collection optics.

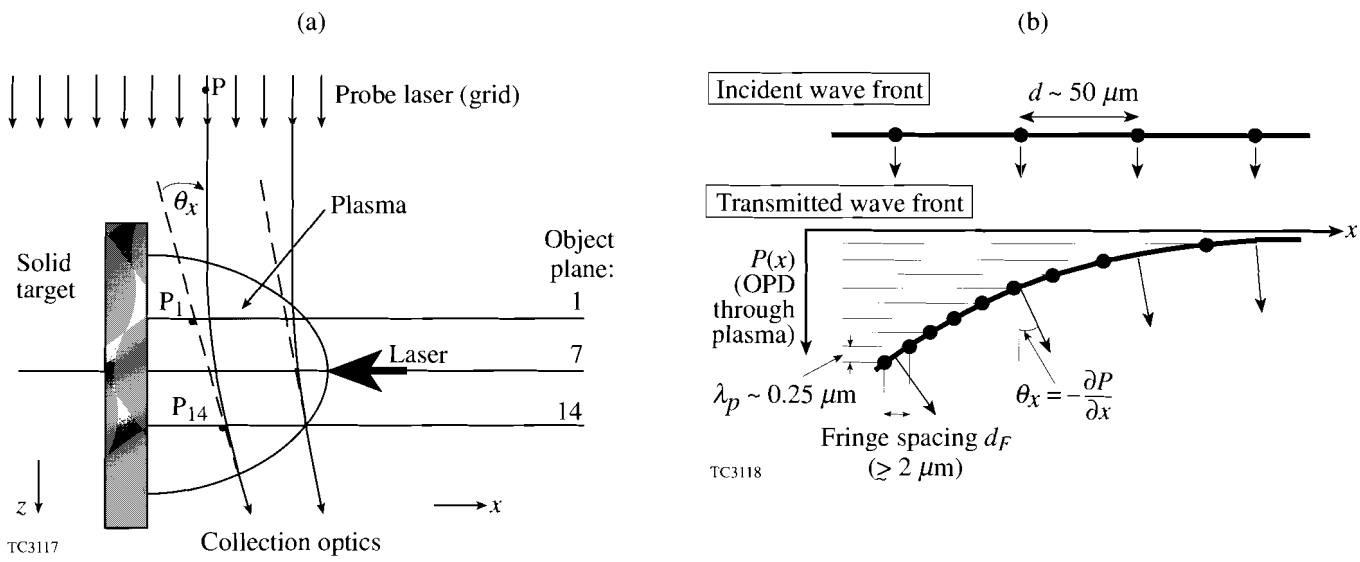

Figure 57.7
(a) Principle of GIR. The apparent position of each probe ray P must be measured for at least two object planes, thereby enabling its deflection angles (θ_x in the x, z plane and θ_y in the y, z plane) to be obtained. (b) Relationship between GIR and interferometry (simplified to omit effects due to strong refraction). In GIR the wavefront $P(x)$ transmitted through the plasma is sampled at uniform intervals (the grid spacing d) in x while, with interferometry, data are obtained each time $P(x)$ changes by the probe wavelength λ_p.

object plane being imaged, the ray will appear to come from points such as P_1 or P_{14}. Provided that images are obtained in a minimum of two such object planes, the angles θ_x and θ_y are calculated very simply by dividing the measured differences of x and y coordinates in the images by the (known) distance between the object planes.

In the present experiment, in which the use of holographic recording provided images for multiple object planes, a more accurate determination of θ_x and θ_y was possible using a least-squares fit to the positions P_i. However, holography shares many of the problems of interferometry, in particular the need for short exposure times to avoid blurring the interference pattern, so that for applications to plasmas with longer scale lengths, such as plasmas anticipated for the OMEGA Upgrade, holography is best avoided. A preferable system would include, instead, a means for directly recording two (or more) images on each shot corresponding to different object planes. This could be accomplished by the insertion of a beam splitter near the film plane of Fig. 57.5(a) and the use of two cameras focused to different object planes. It should be noted that the ability of the holographic system to handle multiple, time-staggered probe pulses[15] would be lost with the GIR system proposed here, which would accommodate a single probe pulse.

The close relationship between GIR and interferometry is illustrated in Fig. 57.7(b) for the case where curvature of the ray path through the plasma can be neglected. (This approximation will be discussed in the following two paragraphs.) Here, the plasma converts a plane incident wave front into a curved transmitted wave front $P(x)$, where $P(x) = \int (1-\mu) ds$ is the optical path difference through the plasma of a ray entering the plasma with impact parameter x. [The refractive index μ in the plasma is equal to $\left(1 - n_e/n_{cp}\right)^{1/2}$, where n_{cp} is the critical electron density corresponding to the probe wavelength, and s measures distance along the ray path.] The difference between the two techniques lies in the way this wave front is sampled. With GIR, sampling occurs every grid spacing d in x; with interferometry, data are obtained every time $P(x)$ changes by λ_p. (It is assumed that, with interferometry, it is feasible to extract only the fringe locations and not information based on intensity variations between fringes.) With GIR the phase-front normal, $\left(\theta_x, \theta_y\right) = \left(-\partial P/\partial x, -\partial P/\partial y\right)$, is measured directly; with interferometry, θ_x is given from the local fringe spacing d_F by $\theta_x = \tan^{-1}\left(\lambda/d_F\right)$. With GIR the phase P is obtained by integrating θ_x along x from vacuum, or by integrating θ_y along y; with interferometry, this integration is performed simply by counting fringes from the outermost fringe. The maximum plasma density that is in principle accessible is

the same in both cases, and a function solely of the f number of the collection optic. In both cases the field of view should be sufficient, to allow a clear zero for the integration of (θ_x, θ_y) in GIR and to allow for the identification of the first fringe in interferometry.

The picture shown in Fig. 57.7(b) is slightly simplified since it is really the emerging phase front as projected back to the appropriate object plane that is imaged onto the plane in which the interferogram is formed. As with grid images such as those of Fig. 57.6, interferograms are dependent on the object plane. This problem has been known for a long time[3,12] and has led to considerable difficulties in the interpretation of experimental interferograms, especially those showing profile steepening and other features around the critical density for 1-μm laser irradiation.[13,29] The problem is minimized by focusing on the plane containing the plasma axis,[3] and it is notable that the difficulties associated with focusing conventional interferometers to the necessary accuracy led to the introduction of holographic interferometry for laser-produced plasmas[30] because then, as with the GIR experiment described in this article, the object plane can be varied during reconstruction.

Even correct focusing is not a complete solution to the problem of reconstructing the density profile. Regardless of whether GIR or interferometry is being used, further errors are introduced by the Abel inversion procedure. This is always carried out in a two-dimensional plane, usually perpendicular to the irradiating laser axis (assumed to be an axis of symmetry). Usually it is assumed, with some justification,[3] that $P(x)$ corresponds to an integral of $(1-\mu)$ along a straight-line path in this plane. Refraction in this plane could be included exactly if the experimental measurement were the refraction angle as a function of impact parameter,[31] but this is not usually the case. However, significant error can arise due to refraction out of the plane of Abel inversion, the dominant refractive effect for steep density profiles, and it may then be preferable to simulate the interferogram directly.[17] Fortunately, Abel inversion is applicable to a good approximation to the experiment reported in this article and to long-scale-length plasmas in general since the lateral displacement of the ray is smaller than the plasma-density scale length (see Ref. 1, Appendix B).

Data Reduction

The data reduction proceeded in two stages: first, the refraction angles (θ_x, θ_y) were extracted; then the plasma density was obtained under the assumption of cylindrical symmetry.

The first stage is illustrated in Fig. 57.8; a typical hand-digitized grid image [corresponding to Fig. 57.6(b)] is shown in Fig. 57.8(a). (The grid-point centers were located by eye on the original photographs and entered into a computer using a digitizer pad.) After the photographs were digitized, it was discovered that two were identical. Their digitizations are superposed in Fig. 57.8(a). The close correspondence indicates that the photographs could be repeatably digitized, even though the image quality and contrast degraded around the periphery. Even though diffractive effects were evident in the images, the locations of the cell centers could be accurately found. In order to register all images on a common coordinate system (x',y'), it was assumed that three grid points, labeled A–C and easily identified in each image, were invariant—points A and B because they were behind the target and point C because it was sufficiently far to the right of the plasma. In this way the varying orientations and translations of the images as placed on the digitizer pad and the varying magnifications of the images could be accounted for. At a later stage it became apparent that the experimental field of view was too small and the ray through point C must have had a non-zero deflection angle. A value of $\theta_x = 0.75°$ was adopted as a plausible deflection for this point (see later). A more accurate registration of the images would obviously have been possible had comparison images been obtained from a reference, plasma-free shot.

Each point in each image was assigned unique (i,j) coordinates. For each (i,j) point it was then possible to plot the apparent (x',y') position in the image as a function of object plane position z and extract the slopes (θ_x, θ_y) using a least-squares fit [see Fig. 57.8(b)]. These angles were obtained without knowing which value of z corresponded to the center of the plasma; it was sufficient to know the spacing between images (100 μm). With the exception of a few points around the periphery of the image where the probe-beam intensity was weak, good straight-line fits were obtained for all (i,j) points. Results with nearly the same accuracy could evidently have been obtained from just two images separated by ~1 mm.

The (x',y') coordinates of Fig. 57.8(a) are arbitrary, and for comparison to be made with *SAGE* simulations a translated coordinate system (x,y) was defined. The choice $x = x' - 100$ μm enabled the closest comparison to be made with the simulations below, and the choice $y = y' - 850$ μm was made so that $y = 0$ corresponded to the axis of symmetry as could best be determined experimentally. The uncertainty in the horizontal shift would of course have been removed if

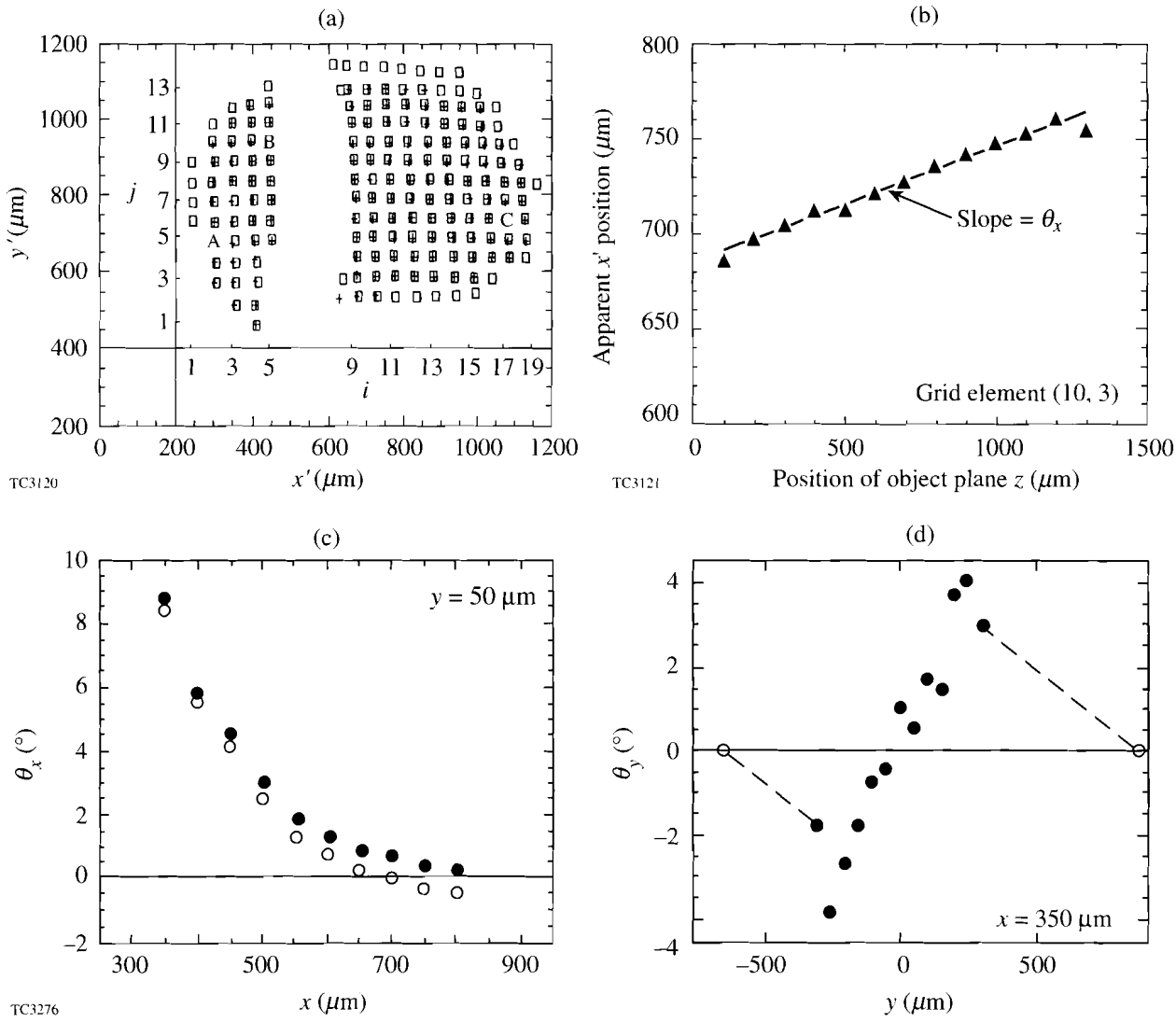

Figure 57.8
Extraction of deflection angles from the grid images. (a) Typical digitized image, with two identical images superposed to illustrate the repeatability of the digitization. All 13 images were then scaled to a common coordinate system (x', y') using reference points A, B, and C. (b) Apparent x' position as a function of object plane position z for a typical grid element. A least-squares fit to the 13 points yields the slope of the ray, θ_x. (c) Lineout of θ_x as a function of x for $y = 50$ μm. Solid (open) points were obtained assuming $\theta_x = 0.75°$ (0°) at reference point C. (d) Lineout of θ_y as a function of y for $x = 350$ μm. Dashed lines indicate extrapolations used outside the experimental field of view.

reference images (of the target and grid in the absence of a plasma) had been available.

Typical lineouts of $\theta_x(x)$ and $\theta_y(y)$ are shown in Figs. 57.8(c) and 57.8(d), respectively. The θ_x lineout, taken approximately along the laser axis, shows why it was necessary to assign a finite deflection angle to point C: the resulting curve (solid circles) asymptotes to zero. If point C were assumed to have no deflection angle (open circles), unphysical negative values of θ_x would be found at large x. The largest standard deviation obtained from least-squares straight-line fits is ±0.25° in θ_x for the point with $\theta_x \approx 9°$, and ≤ ±0.5° for the leftmost and rightmost solid θ_y points. The standard deviation for all other points is less than the symbol size used in the plots. The θ_y lineout, taken at the smallest x (350 μm) at which data existed, reveals an inadequate experimental field of view in the y direction: while θ_y should tend to zero at large $|y|$, the maximum θ_y is observed near the edge of the image. (Further discussion of this problem follows.)

Contour plots of θ_x and θ_y are shown in Fig. 57.9, where experimental and simulated contours are compared. All con-

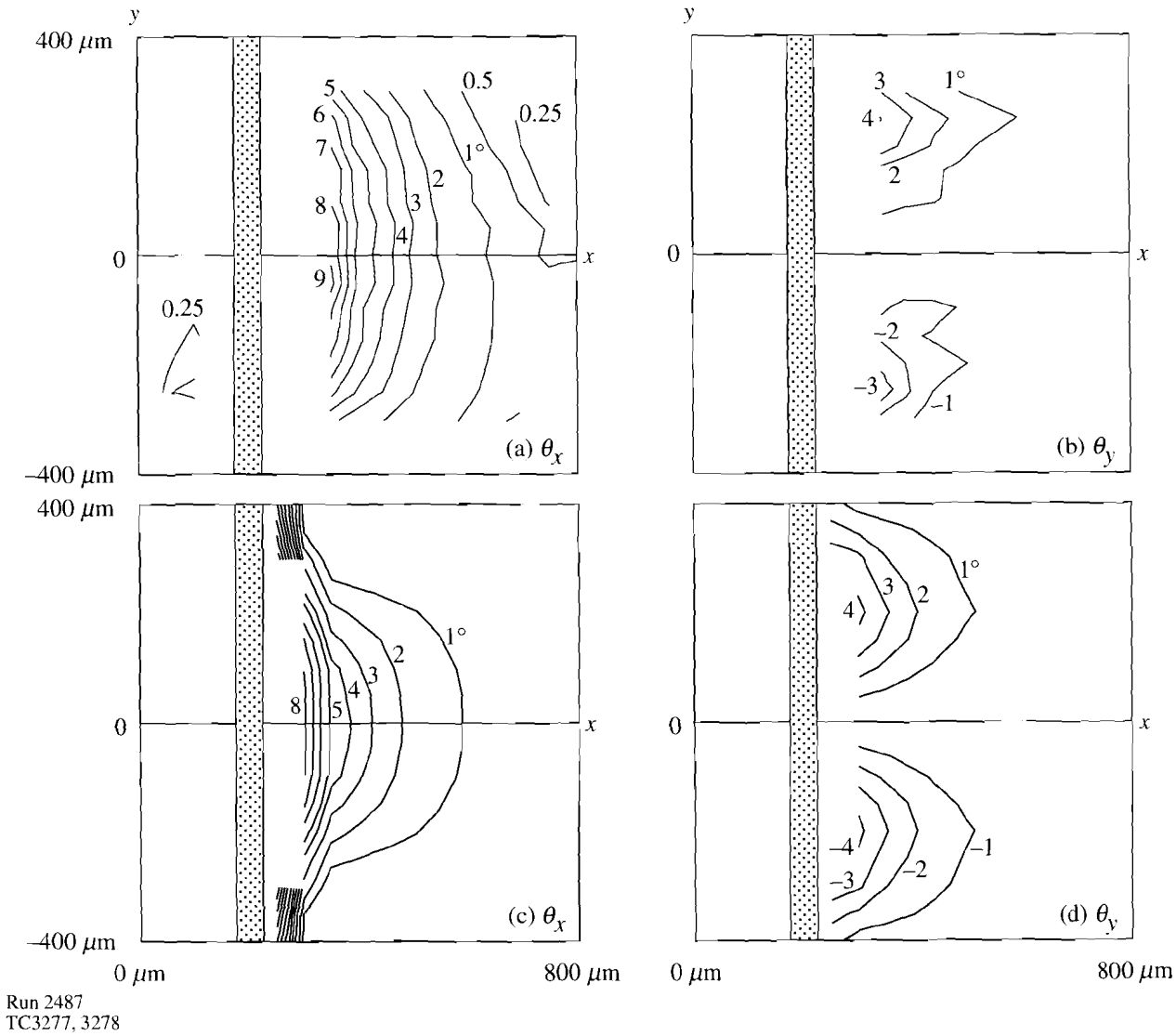

Figure 57.9
Comparison of measured and calculated refraction angles: (a) θ_x and (b) θ_y from GIR; (c) θ_x and (d) θ_y from *SAGE*. The actual positioning of the experimental data relative to the initial solid target (shaded area) and the x axis is unknown. The simulations were performed in cylindrical geometry with x and y the axial and radial coordinates, respectively.

tours are in 1° intervals, except for two additional experimental contours at 0.5° and 0.25°. Reasonable agreement is found for many features of the contours. The main difference appears to be that the experimental contours extend further in the radial (y) direction. The experimental asymmetry seen especially in the 0.5° and 0.25° contours is probably not due to a plasma asymmetry, as discussed above. The least-squares fitting procedure was also applied to the undistorted grid points behind the target, and the 0.25° contour behind the target thus indicates the error associated with the digitization process as applied to the current experimental data.

The second stage of data reduction is illustrated in Fig. 57.10. The phase P was calculated in two ways: integrating θ_x along x to yield P_x, and integrating θ_y along y to yield P_y. Ideally, both P_x and P_y should be equal. However, as observed above, values of θ_y were not available at sufficiently large y, and integration of θ_y from the largest y for which data existed ($y = y_{edge}$, say) yielded values of P_y that in some cases were as low as $0.5\,P_x$. To resolve this problem, a constant was added to each such integral to represent the integral from y_{edge} to ∞, such that P_y matched P_x at $y = 0$.

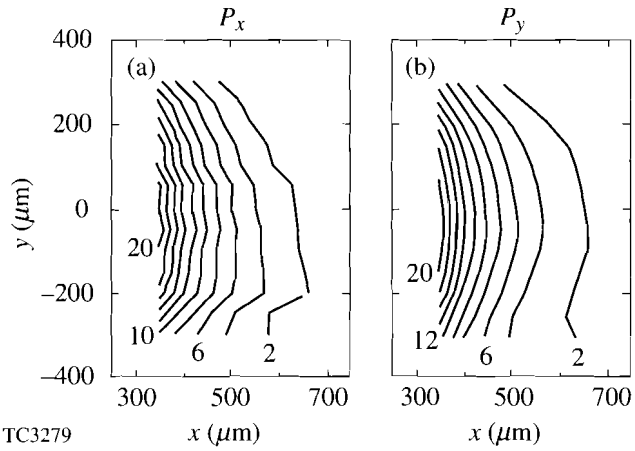

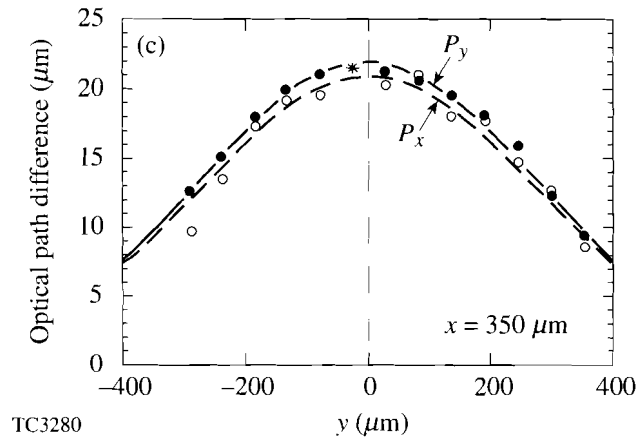

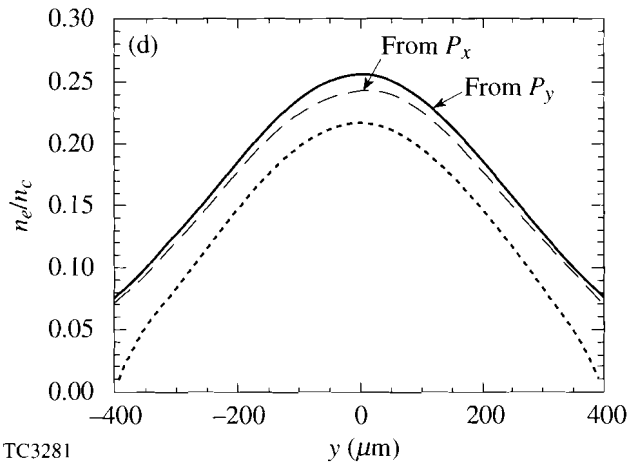

Figure 57.10
Extraction of density profile from θ_x and θ_y. (a) and (b): Contours of phase (optical path difference in microns) obtained by integrating θ_x with respect to x to obtain P_x and θ_y with respect to y to obtain P_y. For each value of x, a Gaussian was found to provide a good fit to the y dependence of P_x and P_y. (c) P_x (open circles) and P_y (solid circles) as functions of y for $x = 350$ μm, together with Gaussian fits about $y = 0$. P_y was forced to equal P_x at the maximum (asterisk) by the appropriate choice of dashed line in Fig. 57.8(d), but the x and y data were otherwise totally independent. (d) Electron-density profile from Abel inversion of the Gaussian fits to P_x and P_y. The dotted curve results from truncating the Gaussian for P_x to zero at $|y| \geq 400$ μm.

Contours of P_x, for which the field of view was (just) adequate, and P_y, adjusted as described, are shown in Figs. 57.10(a) and 57.10(b). The contours have been forced to agree at $y = 0$, but otherwise their shapes correspond very closely. This is notable since, aside from the adjustment, P_x and P_y have been obtained independently from the x and y coordinates of the digitization. This correspondence confirms the self-consistency that the digitized data should possess. It is also worth noting that an interferogram could be simulated simply by plotting contours every 0.26 μm (the probe wavelength) in P rather than every 2 μm. The fringe count at the center would be 80, substantially more than has previously been reported for the interferometric determination of a laser-produced plasma-density profile.

The correspondence between P_x and P_y is shown in Fig. 57.10(c) for the line $x = 350$ μm (the line corresponding to the highest densities that could be probed). Solid circles correspond to P_y and open circles to P_x. The asterisk indicates the point at which P_y was forced to equal P_x. The solid and dashed lines indicate least-squares Gaussian fits to P_y and P_x, respectively. These fits were obtained for each line on the grid, and good symmetry was found with respect to $y = 0$. These curves were then Abel-inverted to yield the density profiles shown in Fig. 57.10(d). By fitting the phase data to smooth curves (Gaussian and truncated Gaussian), problems associated with the differentiation of experimental data were avoided.[4] It is questionable whether the Gaussian fits of Fig. 57.10(c) should be extrapolated to ∞ [leading to the upper curves of Fig. 57.10(d)] or truncated to zero at $|y| = 400$ μm (giving the dotted curve) since $|y| = 400$ μm was in any case outside the field of view. It is likely that the actual density profile lies somewhere in between. This uncertainty was the greatest for the value of x shown here, but even so it did not make a large difference in the density of ~ 0.25 n_c obtained for $y = 0$. The Abel inversions were carried out numerically in all cases, although the Gaussian inverse is known analytically to be a Gaussian.

One interesting difference between the contours of P_x and P_y shown in Fig. 57.10 may be noted: the P_x contours include some fine structure, correlated along horizontal lines, similar to the fine structure in the contour plot of θ_x [Fig. 57.9(a)]. Integration of θ_x along horizontal lines preserves this structure, whereas integration of θ_y perpendicular to these lines evidently does not. It is probable that this structure is physical and results from hot spots in the laser, as similar structures can be seen in interferograms obtained on the CHROMA laser reported in Ref. 32 (and reproduced in Ref. 17). Also, the experimental determination of θ_x is carried out independently for each grid point, so that it would be hard to explain the θ_x correlations seen in Fig. 57.9(a) as noise resulting from the data-reduction process.

Comparison with Simulations

Contours of electron density resulting from the Abel inversion are compared with the predictions of five *SAGE* simulations in Fig. 57.11. The simulations included the *SESAME* equation of state,[33] a multigroup diffusion model for radiation transport (which led to some minor heating of the target surface as seen near $y = 400$ μm),[34] and ray tracing for the incident laser.[20] The experimental contours, shown as heavy lines, are the same in each case: the dashed lines corresponding to extrapolation of the Gaussian fit for $P(y)$ to infinity and the solid lines to truncation at $|y| = 400$ μm. As discussed above, the difference between these lines should be indicative of the experimental uncertainty associated with the restricted field of view in the y direction. In each figure it is the contours

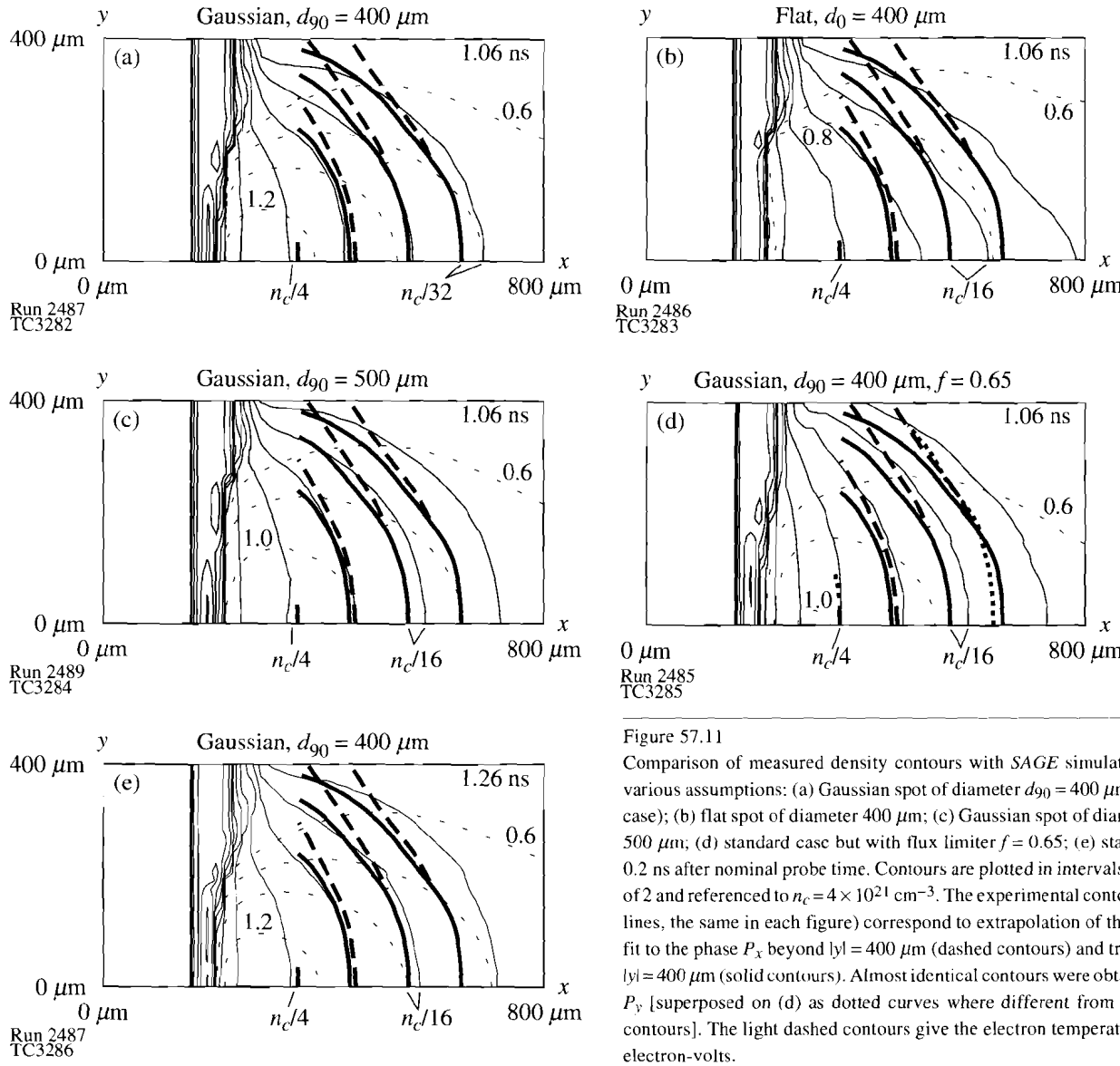

Figure 57.11
Comparison of measured density contours with *SAGE* simulations under various assumptions: (a) Gaussian spot of diameter $d_{90} = 400$ μm (standard case); (b) flat spot of diameter 400 μm; (c) Gaussian spot of diameter $d_{90} = 500$ μm; (d) standard case but with flux limiter $f = 0.65$; (e) standard case 0.2 ns after nominal probe time. Contours are plotted in intervals of a factor of 2 and referenced to $n_c = 4 \times 10^{21}$ cm^{-3}. The experimental contours (heavy lines, the same in each figure) correspond to extrapolation of the Gaussian fit to the phase P_x beyond $|y| = 400$ μm (dashed contours) and truncation at $|y| = 400$ μm (solid contours). Almost identical contours were obtained using P_y [superposed on (d) as dotted curves where different from the dashed contours]. The light dashed contours give the electron temperature in kilo-electron-volts.

based on P_x that are plotted. The contours based on P_y were almost identical, as is seen in Fig. 57.11(d) where they are superposed, where different, as dotted curves.

Starting with Fig. 57.11(a), for a "standard" simulation with a Gaussian focal spot of diameter $d_{90} = 400$ μm, agreement with experiment is for the most part very close. As discussed above, the lack of an experimental determination of the target location relative to the grid allowed the contours to be moved in the x direction (through the transformation from x' to x) to provide the best fit. However, the contour spacing and shapes match remarkably well. A minor discrepancy is seen at the $n_c/32$ contour, where the experimental contour interval (between $n_c/16$ and $n_c/32$) seems to be smaller than predicted. Since this could be related to the choice of 0.75° assumed for θ_x at the reference point C, it is impossible in the absence of a reference shot to say whether or not this discrepancy is real. The main discrepancy is seen at the larger radii, where the experimental plasma seems to have a greater radial extent, even if the solid experimental contours are used. The greatest discrepancy is seen at radii beyond 300 μm, the largest radius in the experimental field of view. It is of interest to ascertain whether or not such a discrepancy could yield insight into physical processes such as thermal transport, and it is worth noting that a similar motivation for comparing simulated and experimental interferograms is found in Ref. 17. The following plots of Fig. 57.11 are included to show that there could be a variety of explanations for the discrepancy aside from thermal transport modeling.

The simulation of Fig. 57.11(b) assumes a flat focal spot, also of diameter 400 μm. The predicted blowoff in this case is strongly peaked in the direction of the target normal, and the match at low densities, especially around $n_c/32$, is much poorer. The reason for the different coronal shape may be readily understood from the temperature contours, shown as light dashed lines. For the flat focal spot the plasma temperature and expansion are fairly uniform in y, and the expansion velocity is initially in the $+x$ direction. Not until the combination of a rarefaction wave and a thermal wave feeds in from the edge of the spot does the plasma near the x axis see a nonzero radial pressure gradient and start to expand radially. For the Gaussian spot, radial temperature (and pressure) gradients are always present.

In Fig. 57.11(c) results are given for a simulation with a Gaussian beam of slightly bigger diameter (500 μm). Here the discrepancy at large y has almost vanished, especially for the solid experimental curves. Unfortunately the precise focal intensity distribution in the experiment was not known; thus it is entirely possible that the observed discrepancy is due primarily to an insufficiently precise knowledge of the focal spot.

Figure 57.11(d) presents the standard simulation but with a flux limiter[35] f of 0.65. (A value of 0.04 was used in the other simulations.) This led to the desired increase in the radial plasma size but also produced a more extended plasma in the x direction. One other possibility—a timing discrepancy of 0.2 ns between simulation and experiment—is investigated in Fig. 57.11(e). At the later time (1.26 ns) the predicted plasma is bigger, as expected, and has density contours comparable to those produced by the larger flux limiter. Thus, in order to make a strong statement about thermal transport, a good timing fiducial and an accurate knowledge of experimental parameters, such as the focal spot profile, are essential.

Conclusions

A new technique—grid image refractometry (GIR)—has been proposed for the determination of density profiles in underdense plasmas. The method has much in common with classical Schlieren techniques and other forms of refractometry, but includes some unique features that make it especially applicable to laser-produced plasmas where ray deflection angles can be large. GIR has significant advantages over interferometry for long-scale-length plasmas such as will be produced on the OMEGA Upgrade and, in particular, does not depend on probe-beam coherence and does not require inconveniently short probe times. (The probe duration for GIR should not exceed the time scale of plasma hydrodynamic motion, which is much greater than the fringe-blurring time.) The price paid is the loss of spatial resolution on the micron scale length, but, for the plasmas of interest, this is not particularly important. The feasibility of the method has been demonstrated by an experiment carried out on the CHROMA laser.

Even though experimental data were available just for a single shot, it has been possible to extract two-dimensional density profiles that extend up to $n_e = 10^{21}$ cm^{-3} and compare very well with hydrodynamic simulations. Few, if any, such detailed comparisons have been previously reported. For future applications to long-scale-length plasmas, it is proposed to replace the holographic system with a beam splitter and a recording system that will enable two (or more) images, corresponding to different object planes, to be recorded directly on a single shot. This should eliminate problems associated with temporal smearing of the holographic pattern.

GIR can in principle be used to investigate physical processes such as electron thermal transport, but only if an accurate knowledge of laser and target conditions is available. In addition, if a measurement were made of probe-beam attenuation across the same field of view (resulting from inverse bremsstrahlung), it would be possible to determine the electron-temperature profile in the plasma as well as the electron-density profile.

A knowledge of the density profile of long-scale-length plasmas is very important to the understanding of plasma physics issues relevant to inertial-confinement fusion. GIR seems to be a very attractive method with considerable promise for the diagnosis of millimeter-scale-length plasmas.

ACKNOWLEDGMENT

This work was supported by the U.S. Department of Energy Office of Inertial Confinement Fusion under Cooperative Agreement No. DE-FC03-92SF19460 and the University of Rochester. The support of DOE does not constitute an endorsement by DOE of the views expressed in this article. This work was also supported by the Laboratory for Laser Energetics' Summer High-School Program, which was partially funded by the National Science Foundation Grant No. RCD9055084.

REFERENCES

1. R. S. Craxton, F. S. Turner, R. Hoefen, C. Darrow, E. F. Gabl, and Gar. E. Busch, Phys. Fluids B **5**, 4419 (1993).
2. F. B. Hildebrand, *Methods of Applied Mathematics*, 2nd ed. (Prentice-Hall, NJ, 1965), p. 276.
3. C. M. Vest, Appl. Opt. **14**, 1601 (1975).
4. M. Deutsch, Appl. Phys. Lett. **42**, 237 (1983).
5. D. T. Attwood, D. W. Sweeney, J. M. Auerbach, and P. H. Y. Lee, Phys. Rev. Lett. **40**, 184 (1978).
6. A. Raven and O. Willi, Phys. Rev. Lett. **43**, 278 (1979).
7. C. B. Darrow *et al.*, Phys. Fluids B **3**, 1473 (1991).
8. W. Seka, R. S. Craxton, R. E. Bahr, D. L. Brown, D. K. Bradley, P. A. Jaanimagi, B. Yaakobi, and R. Epstein, Phys. Fluids B **4**, 432 (1992); see also Laboratory for Laser Energetics LLE Review **47**, Quarterly Report No. DOE/DP/40200-166, 1991 (unpublished), p. 109.
9. B. J. MacGowan *et al.*, Bull. Amer. Phys. Soc. **38**, 1934 (1993), paper 3E 1.
10. H. Azechi *et al.*, Phys. Rev. Lett. **39**, 1144 (1977).
11. R. E. Turner and L. M. Goldman, Phys. Rev. Lett. **44**, 400 (1980).
12. G. J. Tallents, M. D. J. Burgess, and B. Luther-Davies, Opt. Commun. **44**, 384 (1983), and Erratum **45**, 420 (1983).
13. M. D. J. Burgess, G. B. Gillman, and B. Luther-Davies, J. Appl. Phys. **54**, 1787 (1983).
14. R. Fedosejevs, M. D. J. Burgess, G. D. Enright, and M. C. Richardson, Phys. Rev. Lett. **43**, 1664 (1979).
15. Gar. E. Busch *et al.*, Rev. Sci. Instrum. **56**, 879 (1985).
16. J. A. Tarvin *et al.*, Laser Part. Beams **4**, 461 (1986).
17. M. K. Prasad, K. G. Estabrook, J. A. Harte, R. S. Craxton, R. A. Bosch, Gar. E. Busch, and J. S. Kollin, Phys. Fluids B **4**, 1569 (1992).
18. R. R. Johnson *et al.*, Phys. Rev. A **41**, 1058 (1990).
19. R. P. Drake *et al.*, Phys. Fluids **31**, 1795 (1988).
20. R. S. Craxton and R. L. McCrory, J. Appl. Phys. **56**, 108 (1984).
21. L. A. Vasil'ev, *Schlieren Methods* (Israel Program for Scientific Translations, New York, 1971).
22. V. Gurfein *et al.*, Opt. Commun. **85**, 147 (1991).
23. N. Miyanaga, Y. Kato, and C. Yamanaka, Opt. Commun. **44**, 48 (1982).
24. R. Benattar and J. Godart, Opt. Commun. **49**, 43 (1984).
25. O. Kafri, Opt. Lett. **5**, 555 (1980).
26. J. E. Trebes *et al.*, Bull. Am. Phys. Soc. **38**, 2044 (1993).
27. I. Ghozeil, in *Optical Shop Testing*, 2nd ed., edited by D. Malacara (Wiley, New York, 1992), p. 367.
28. J. A. Sell *et al.*, Appl. Phys. Lett. **55**, 2435 (1989).
29. G. Gillman, Opt. Commun. **35**, 127 (1980).
30. D. T. Attwood, IEEE J. Quantum Electron. **14**, 909 (1978).
31. P. W. Schreiber, A. M. Hunter, and D. R. Smith, Plasma Phys. **15**, 635 (1973).
32. G. Charatis *et al.*, J. Phys. (Paris) **47**, C6-89 (1986).
33. B. I. Bennett *et al.*, Los Alamos National Laboratory Report LA-7130 (1978).
34. W. F. Huebner *et al.*, Los Alamos National Laboratory Report LA-6760-M (1977).
35. R. C. Malone, R. L. McCrory, and R. L. Morse, Phys. Rev. Lett. **34**, 721 (1975).